

# We are IntechOpen, the world's leading publisher of Open Access books Built by scientists, for scientists

6,900

Open access books available

186,000

International authors and editors

200M

Downloads

Our authors are among the

154

Countries delivered to

TOP 1%

most cited scientists

12.2%

Contributors from top 500 universities



WEB OF SCIENCE™

Selection of our books indexed in the Book Citation Index  
in Web of Science™ Core Collection (BKCI)

Interested in publishing with us?  
Contact [book.department@intechopen.com](mailto:book.department@intechopen.com)

Numbers displayed above are based on latest data collected.  
For more information visit [www.intechopen.com](http://www.intechopen.com)



# Real-time, Multi-wavelength Holographic Recording in Photorefractive Volume Media: Theory and Applications

Eduardo Acedo Barbosa

*Laboratório de Óptica Aplicada, Faculdade de Tecnologia de São Paulo, CEETEPS – UNESP, Pça Cel Fernando Prestes, 30, 01124-060, São Paulo – SP Brazil*

## 1. Introduction

Due to very interesting properties like reversible recording with unlimited number of recording-erasure cycles, high image resolution and high storage capability, thick photorefractive media have been applied in many areas like information storage (Chuang & Psaltis, 1997), pattern recognition (Alam & Khoury, 2000), phase conjugation (Chang et al, 2001), optical image processing (Poon & Banerjee, 2001) and optical metrology (Georges et al, 2001; Frejlich & Garcia, 2000).

Photorefractive crystals of the sillenite family ( $\text{Bi}_{12}\text{SiO}_{20}$ ,  $\text{Bi}_{12}\text{TiO}_{20}$  and  $\text{Bi}_{12}\text{GeO}_{20}$ ) have characteristics which make them very useful for image processing and for optical metrology, particularly for holographic interferometry (Barbosa & Muramatsu, 1997; Kukhtarev et al, 1993). Those crystals present a relatively short response time, which is very desirable for the field of non-destructive testing, and the typically low diffraction efficiency of these materials can be overcome by taking advantage from their anisotropic diffraction properties (Kamshilin & Petrov, 1985). The  $\text{Bi}_{12}\text{TiO}_{20}$  (BTO) crystals have the additional advantage of a relatively low optical activity for the red light, which allows the highest possible diffraction efficiency for this wavelength range (Frejlich, 2006).

Holographic contouring is generally based on two-exposure recording, i.e. in each exposure the holographic image is recorded with one setup configuration. During the holographic readout the reconstructed waves referent to each object state interfere and thus generate a contour fringe pattern. In two-wavelength techniques (Kuchel & Tiziani, 1981; Millerd & Brock, 1997) the laser is tuned between the exposures, while in other methods the beam illuminating the object is slightly tilted between the first and the second recording (Pedrini et al, 1999; Yamaguchi et al, 2001).

The study and application of holographic processes in sillenite crystals by using multi-wavelength, large free spectral range diode lasers provided the generation of real-time contour interferograms with only one exposure, thus enabling much faster and easier testing. It was shown that the diffracted light intensity strongly depends on the phase difference between the reference and the object beams and on the laser FSR. The holographic image thus appears covered of interference fringes corresponding to the contour lines of the object surface (Barbosa, 2005). By phase-shifting the reference beam, the fringes run along

the surface, thus allowing for quantitative three-dimensional scanning of the object by phase shifting methods. This chapter shows the basic theory and the consequent applications of multi-wavelength holography in thick photorefractive materials. The text is organized as follows: in section 2 the fundamentals of the holographic recording in photorefractive crystals are presented; section 3 shows the basic principles which originate the longitudinal lasers modes and the contour fringe formation when holographic interferometers are illuminated by multimode lasers; section 4 treats on the theory and experiments about two-laser holography, and section 5 describes two applications of multi-wavelength and two-laser holography.

## 2. Holographic recording in thick photorefractive materials

When two coherent, monochromatic waves of wavelength  $\lambda$  interfere at a photorefractive material, the resulting light interference pattern spatially rearranges the charge carriers (electrons or holes) inside the medium by diffusion or drift. The charge carriers are optically excited from filled donors and are recombined to empty traps thus migrating from illuminated to dark regions of the material, resulting in a space-dependent charge distribution. According to Poisson's equation this charge grating generates a spatially periodic electric field  $E_{sc}$ , and through the electrooptic effect (Pockels effect) this space charge field produces a refractive index grating of amplitude  $\Delta n$ . The induced birefringence grating in turn depends not only on the photorefractive medium constants, like e.g. its refractive index and its electro-optic response, but also on experimental parameters, like the angle between the interfering beams and the orientation of the holographic vector with respect to the crystallographic axes, in the case of photorefractive crystals. For instance, in a very common configuration of the  $\text{LiNbO}_3$  crystal one gets  $\Delta n = n_0 r_{33} E_{sc} / 2$ , while for the sillenite crystals ( $\text{Bi}_{12}\text{SiO}_{20}$ ,  $\text{Bi}_{12}\text{TiO}_{20}$  and  $\text{Bi}_{12}\text{GeO}_{20}$ ) cut in the electrooptic transverse configuration one gets  $\Delta n = n_0^3 r_{41} E_{sc} / 2$ , where  $r_{33}$  and  $r_{41}$  are electrooptic coefficients, and  $n_0$  is the bulk refractive index (Frejlich, 2006).

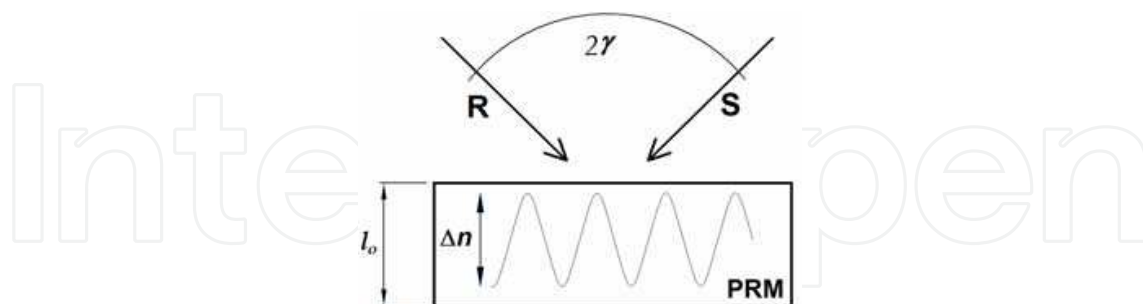


Fig. 1. Incidence of the reference and the object beams onto the photorefractive medium

Due to its simplicity and versatility, the most used optical scheme in holographic interferometry is the dual-beam interferometer which allows simultaneous holographic recording and readout. In this configuration the readout occurs by self diffraction, with the reference wave acting also as the reconstructing wave. Let  $2\gamma$  be the angle between the object and the reference beams interfering at the photorefractive medium (PRM) of thickness  $l_0$ , as shown in Figure 2. According to Kogelnik's coupled-wave theory (Kogelnik, 1969), the diffraction efficiency  $\eta$  of a phase transmission grating is given by

$$\eta = \frac{\sin^2(\sigma^2 + \xi^2)^{1/2}}{1 + (\xi/\sigma)^2}, \quad (1)$$

where  $\sigma \equiv \pi d \Delta n / (\lambda \cos \alpha)$ . The *Bragg factor*  $\xi$  is a measure of how out of Bragg regime the readout process occurs, such that  $\xi = 0$  for perfect Bragg conditions. This parameter will be studied in more detail in the next sections.

In this chapter the holographic process will be analyzed regarding the parameters and the properties of the sillenite crystals. Those materials present typically low values of refractive index modulation  $\Delta n$  (in the order of  $10^{-5}$ ), hence  $\sin \sigma \approx \sigma$ . In the most experiments of homodyne holographic interferometry the perfect Bragg condition is automatically fulfilled, so that equation (1) becomes simply  $\eta \cong \sigma$ . This latter parameter in turn was calculated considering the cut of the sillenite crystals in the [110] electrooptic transverse configuration to be (Mallick & Rouède, 1987)

$$\eta_0 = \left( \frac{n_0^3 r_{41} E_{sc} \sin \rho l_0}{2 \lambda \cos \gamma \rho l_0} \right)^2 \quad (2)$$

where  $\rho$  is the crystal rotatory power. In this case, the anisotropic diffraction properties of the sillenite crystals and their optical activity can be explored in order to make the transmitted and the diffracted waves orthogonally polarized at the crystal output, provided the input wave polarization is selected to be parallel to the [001] axis half-way through the crystal (Kamshilin & Petrov, 1985). Thus, by blocking the transmitted object wave by a polarizer the holographically reconstructed object image only can be visualized.

In multi-wavelength holography the Bragg conditions are often not obeyed; in some experiments of wavefront reconstruction by two-laser holography the parameter  $\xi$  can be significantly larger than  $\sigma$ , so that from equation (1) the diffraction efficiency assumes the form

$$\eta = \eta_0 \frac{\sin^2 \xi}{\xi^2} \quad (3)$$

Equation (3) shows that the diffraction efficiency  $\eta$  equals the perfect Bragg value  $\eta_0$  for  $\xi = 0$  and becomes smaller than unit in off-Bragg regimes, falling down to 0 for  $\xi = \pi$  rad.

### 3. Holographic imaging and wavefront reconstruction with a single multimode laser

#### 3.1 Longitudinal modes of large bandwidth, large free spectral range lasers

The resonator of the diode lasers can be regarded basically as a Fabry-Perot étalon or interferometer with the gain medium inside. The electromagnetic field originated from the gain medium oscillates between the two plane and parallel mirrors of the étalon, being partially reflected, partially transmitted every time it bounces one of the mirrors. The spectrum of a radiation field transmitted through an étalon filled with a passive (i.e. non-amplifying) medium indicates the wavelengths which may oscillate inside the laser resonator. From the basic Fabry-Perot theory the relation between those wavelengths and the resonator  $L$  is given by (Hecht, 1998)

$$L = q \frac{\lambda}{2}, \quad (4)$$

where  $q = 1, 2, 3, \dots$ . Hence, when such an étalon is the cavity of a inhomogeneously broadened laser (Koechner, 1998), the waves obeying equation (4) comprise the *longitudinal modes* of this laser. The free spectral range (FSR)  $\Delta\nu$  is the spectral interval between two adjacent modes and can be written with the help of equation (4) and the relation  $c = \nu\lambda$  as

$$\Delta\nu = \nu_{q+1} - \nu_q = \frac{c}{2L}, \quad (5)$$

where  $c$  is the light velocity inside the medium. The corresponding wavelength difference is then given by

$$\Delta\lambda = \frac{\lambda^2}{c} \Delta\nu = \frac{\lambda^2}{2L} \quad (6)$$

### 3.2 Holographic recording and readout with a multimode laser; contour fringe formation

Let us now consider both the reference and the object waves originated from a multimode laser with  $N$  longitudinal modes. At the holographic medium input, the reference ( $R_N$ ) and the object ( $S_N$ ) beams can be expressed as

$$R_N = R_0 \sum_{q=-(N-1)/2}^{q=(N-1)/2} A_q e^{i[(k+q\Delta k)\Gamma_R + \phi_q]} \quad (7)$$

$$S_N = S_0 \sum_{q=-(N-1)/2}^{q=(N-1)/2} A_q e^{i[(k+q\Delta k)\Gamma_S + \phi_q]}$$

where  $k \equiv 2\pi/\lambda$ ,  $\Delta k = 2\pi\Delta\lambda/\lambda^2$  is the wavenumber gap between two adjacent modes,  $A_q$  is a real coefficient associated to the amplitude of each longitudinal mode and  $\phi_q$  is the phase of the  $q$ -th mode at the laser output.  $\Gamma_S$  and  $\Gamma_R$  are the optical paths of the object and the reference beams at the crystal, respectively.

In the absence of an externally applied electric field on the photorefractive crystal the charge transport occurs only by diffusion. The space charge electric field  $E_{sc}$  is then given by

$$E_{sc} \cong imE_D \equiv iE_D \frac{2R_N^* S_N}{I_0} \quad (8)$$

where  $m$  is the modulation of the interference pattern,  $I_0 = |R_N|^2 + |S_N|^2$  and  $E_D$  is the electric field generated by diffusion. The symbol  $*$  denotes complex conjugation.

Each mode (i.e., each wavelength) contributes to the holographic recording with its own hologram and therefore the resulting grating is a superposition of all holograms. Since different modes are not mutually coherent, the phase difference  $\phi_q - \phi_p$  ( $q \neq p$ ) has a random behaviour in time. Thus, the interference of different modes does not contribute to the holographic recording, being only responsible for a background light which lowers the grating amplitude  $\Delta n$  and consequently decreases the overall hologram diffraction

efficiency. Hence, from equations (7) and (8) the diffraction efficiency can be expressed through the following matrix product:

$$\eta = \eta_0 \left| i e^{ik(\Gamma_S - \Gamma_R)} \sum_{p=-(N-1)/2}^{p=(N-1)/2} \sum_{q=-(N-1)/2}^{q=(N-1)/2} \delta_{p,q} A_p A_q e^{i\Delta k(p\Gamma_S - q\Gamma_R)} \right|^2 \Rightarrow$$

$$\eta = \eta_0 \left| \sum_{n=-(N-1)/2}^{n=(N-1)/2} A_n^2 e^{in\Delta k(\Gamma_S - \Gamma_R)} \right|^2 \quad (9)$$

where  $\eta_0 \equiv \left( \frac{n_0^3 r_{41} E_D R_0 S_0 \sin \rho l_0}{2\lambda \cos \gamma I_0 \rho l_0} \right)^2$  is the unmodulated diffraction efficiency.

In self-diffraction, each mode is diffracted by all the holograms. Thus, for  $N$  longitudinal laser modes, there are  $N$  recorded gratings and  $N^2$  diffracted waves. The diffracted waves originated from the same mode add coherently and are responsible for the fringe formation while the diffracted beams originated from different modes add incoherently (addition of wave intensities). This can be mathematically expressed by writing the amplitude of the diffracted wave as a function of the square root of the diffraction efficiency. Let us consider the example in which the multiple holograms result from the interference of waves originated from a three-mode diode laser. When the volume hologram is illuminated by the reference wave  $R = R_0 A_0 e^{ik\Gamma_R}$  (which correspond to the 0-th mode of the laser) the diffracted wave amplitude can then be written as

$$E_D(q=0) = \sqrt{\eta} R_0 e^{ik\Gamma_R}$$

$$= \sqrt{\eta_0} \left( \chi_{-1,0} A_{-1} e^{-i\Delta k(\Gamma_S - \Gamma_R)} + A_0 + \chi_{1,0} A_1 e^{i\Delta k(\Gamma_S - \Gamma_R)} \right) R_0 e^{ik\Gamma_R} \quad (10a)$$

Correspondingly, the diffracted waves due to the incidence of the modes -1 and 1 can be written as

$$E_D(q=-1) = \sqrt{\eta_0} \left( A_{-1} e^{-i\Delta k(\Gamma_S - \Gamma_R)} + \chi_{0,-1} A_0 + \chi_{1,-1} A_1 e^{i\Delta k(\Gamma_S - \Gamma_R)} \right) R_0 e^{i(k-\Delta k)\Gamma_R} \quad (10b)$$

$$E_D(q=1) = \sqrt{\eta_0} \left( \chi_{-1,1} A_{-1} e^{-i\Delta k(\Gamma_S - \Gamma_R)} + \chi_{0,-1} A_0 + A_1 e^{i\Delta k(\Gamma_S - \Gamma_R)} \right) R_0 e^{i(k+\Delta k)\Gamma_R} \quad (10c)$$

The terms  $\chi_{p,q} \equiv \sin \xi_{p,q} / \xi_{p,q}$  take into account the deviations from the perfect Bragg regime. The three diffracted waves from equation (10a) add coherently, and the same occurs with the ones of equations (10b) and (10c). On the other hand, the waves resulting from equation (10a), equation (10b) and equation (10c) add incoherently.

The intensity of the waves diffracted by the volume grating can be obtained in a much more convenient form by making some simplifying assumptions without loss of generality. The parameters of the multimode diode lasers typically lead to values of  $\chi_{p,q}$  very close to 1. Moreover, let us consider the particular case for which  $A_q=1$  in order to simplify the following analysis of surface profilometry. Hence, when the reference beam of intensity  $I_R$  is diffracted by the hologram, the holographic reconstruction of the object beam of intensity  $I_S$  is obtained from equations (8), (9) and (10) as

$$I_D = \eta I_R = \eta_0 \left\{ \frac{\sin[N\Delta k(\Gamma_S - \Gamma_R)/2]}{\sin[\Delta k(\Gamma_S - \Gamma_R)/2]} \right\}^2 I_R \quad (11)$$

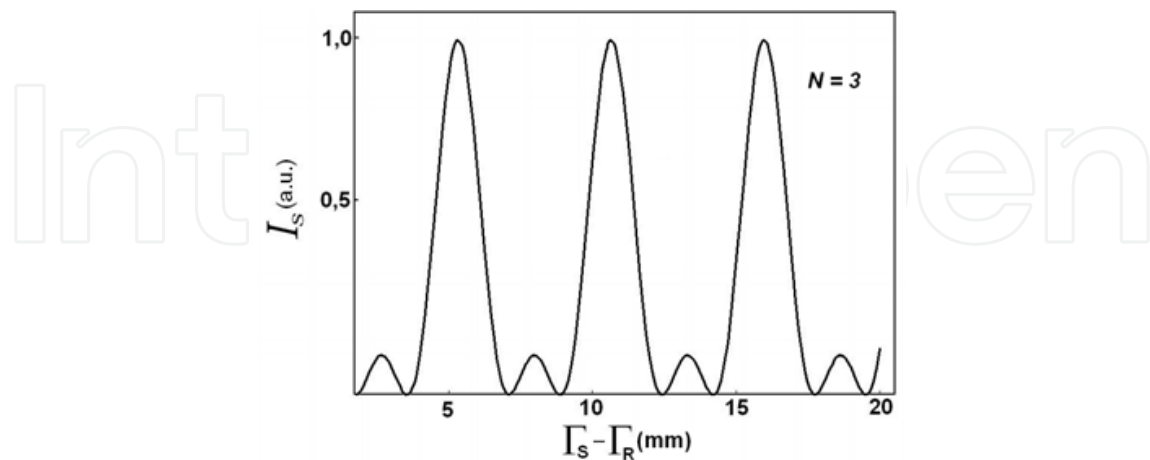


Fig. 2. Intensity of the diffracted wave for  $N = 3$  longitudinal modes

Figure 2 shows the behaviour of  $I_S$  from equation (11) as a function of  $\Gamma_S - \Gamma_R$ , for  $\Delta k = 1.39$  rad/mm and  $N = 3$ . The intensity maxima correspond to the bright fringes on the reconstructed object image. Since the optical path  $\Gamma_S$  depends on the object surface, and considering that the reference beam is a plane wave, one comes to the conclusion that the contour interference fringes are originated from the intersection of the surface with parallel planes of constant elevation. The distance between those planes is closely related to the resulting synthetic wavelength, as will be seen with more detail in the next sections. The analysis of such interference pattern allows the profilometric measurement of three-dimensional surfaces. From equation (11) one determines the difference on the optical paths between any pair of adjacent fringes as a function of the wavelength difference  $\Delta\lambda$ :

$$\Gamma_{S,O} - \Gamma_{S,P} = \frac{2\pi}{\Delta k} = \frac{\lambda^2}{\Delta\lambda} \equiv \lambda_s \quad (12)$$

The term  $\lambda_s$  is called as the *synthetic wavelength*, widely used in heterodyne interferometry. Notice that the synthetic wavelength is directly related to the laser FSR for longitudinal modes given by equation (6), such that  $\lambda_s/2 = L$ . Hence, when long resonator (e.g.  $L > 20$  cm) multimode lasers are employed the contour fringes cannot be visualised for surface depths smaller of tens of centimeters, since the free-spectral range of such lasers is much smaller than that of short-length ( $L \cong 2$  mm, typically) diode lasers.

From equation (11) one sees clearly that the bright contour fringes resulting from multi-wavelength holography do not necessarily present the same form of the usual double-exposure,  $\cos^2$ -fringe patterns. In fact, the width  $\delta\Gamma_S$  of the bright fringe, defined as twice the  $\Gamma_S$  difference from the fringe peak to the first zero, can be easily obtained with the help of equation (15) as  $\delta\Gamma_S = 2/N\Delta k$ . This expression evidences that the higher is the number  $N$  of longitudinal modes, the narrower is the bright fringe. Figure 3a shows the holographic image of a flat metallic bar,  $30^\circ$ -tilted with respect to the front face of the crystal with the expected vertical and parallel contour fringes, while figure 3b shows the interferogram intensity profile along the line A-B from figure 3a. The narrow fringes in the intensity profile

from figure 3b in comparison with the usual  $\cos^2$ -fringes suggests the oscillation of 4 laser modes.

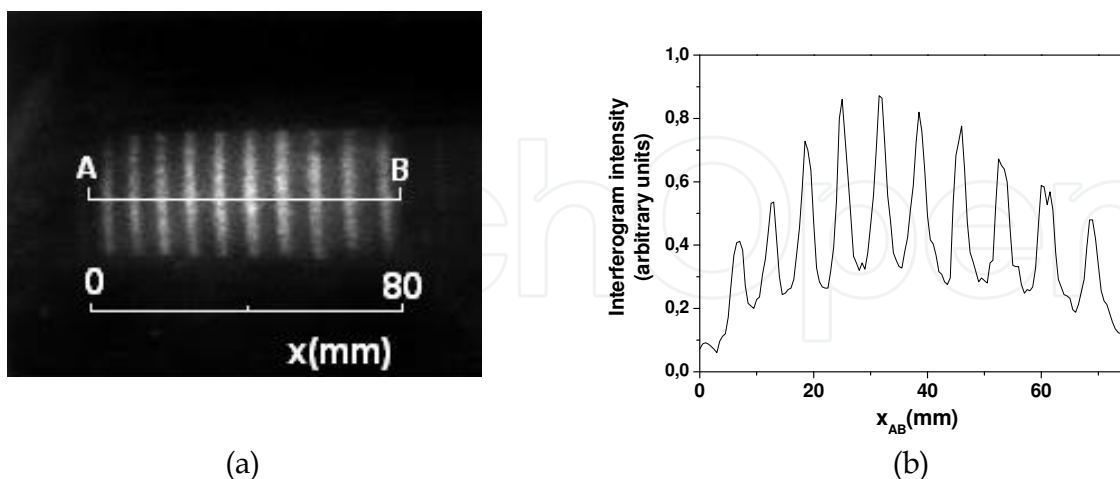


Fig. 3. (a) – Multi-wavelength contour interferogram generated on a flat plate; (b) – intensity profile of the fringe pattern.

The group of phase-shifting techniques for quantitative fringe evaluation is based on the intensity change of the interferogram by phase shifting one of the interfering beams in the holographic setup. In the current case, this is carried out in a four-frame process, through which the reference beam is sequentially 0-,  $\pi/2$ -,  $\pi$ - and  $3\pi/2$ -phase shifted. Thus, from equation (14) the intensity at a point  $(x,y)$  can be conveniently written as

$$I_{D,l}(x,y) = \eta_0 \left\{ \frac{\sin[N(\Delta k \Gamma_S(x,y) + l\pi/2) / 2]}{\sin[(\Delta k \Gamma_S(x,y) / 2 + l\pi/2) / 2]} \right\}^2 I_R, \quad (13)$$

where  $l = 0,1,2$  and 3. Considering  $N = 2$  longitudinal modes of the laser, the relative phase  $\phi_S(x,y) \equiv \Delta k \Gamma_S(x,y)/2$  of the surface can be obtained as a function of the interferogram intensities  $I_{D0}$ ,  $I_{D1}$ ,  $I_{D2}$ , and  $I_{D3}$  according to (Barbosa et al, 2005)

$$\phi_{4\text{-step}}(N = 2) = \arctan \left( \frac{I_{D3} - I_{D1}}{I_{D0} - I_{D2}} \right) \quad (14)$$

From equation (14) one gets a phase map in a grey level intensity, with the range  $-\pi < \phi < \pi$  corresponding to 256 grey levels, from black ( $\phi = -\pi$ ) to white ( $\phi = \pi$ ).

The arctan function has a period of  $2\pi$  rad and therefore it is not possible do directly determine the whole phase which exceed this range of  $-\pi$  to  $\pi$  rad. For this reason the phase obtained from the equations above is said to be “wrapped”. In order to unwrap the phase map – or make its deconvolution -obtained through equation (14) several methods were applied in the literature, like the cellular-automata (Ghiglia et al) and the branch-cut methods (Gutmann & Weber, 1999).

### 3.3.1 Example of shape measurements

*Profilometry by four stepping method* – figure 4 shows a typical dual-beam optical setup employed for holographic profilometry experiments. The reference and the object beams

interfere at the BTO crystal after passing through the polarizer P1. The object is imaged onto the BTO crystal by lens L1, while the reconstructed object wave is collected by lens L2 to build the holographic object image at the CCD camera. The crystal is cut in the [110] transverse electro-optic configuration in order to take advantage from the anisotropic diffraction properties of the sillenite crystals as described in section 2. The transmitted object beam is thus blocked by analyzer P2 so that only the holographic image is displayed in a computer monitor for further processing. The 90°-prism PR is attached to a micrometer and translated in order to introduce the phase shift in the reference beam for the four-stepping procedure.

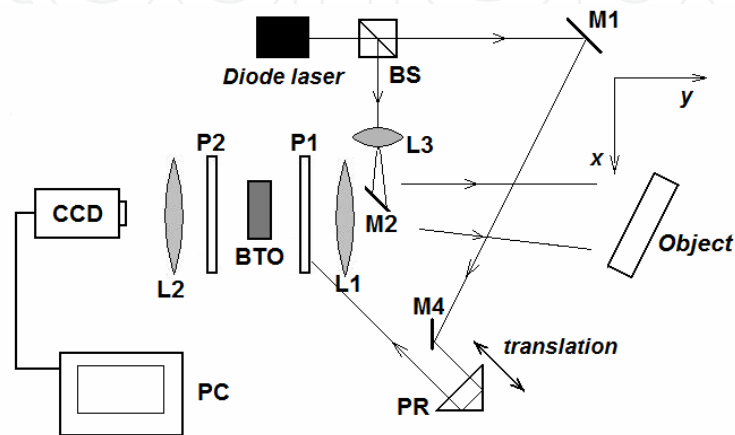


Fig. 4. Holographic setup. L1 to L3, lenses; M1 to M4, mirrors; BS, beam splitter; P1 and P2, polarizers; BTO, holographic storage medium; PR, 90°-prism; CCD, camera; PC, computer

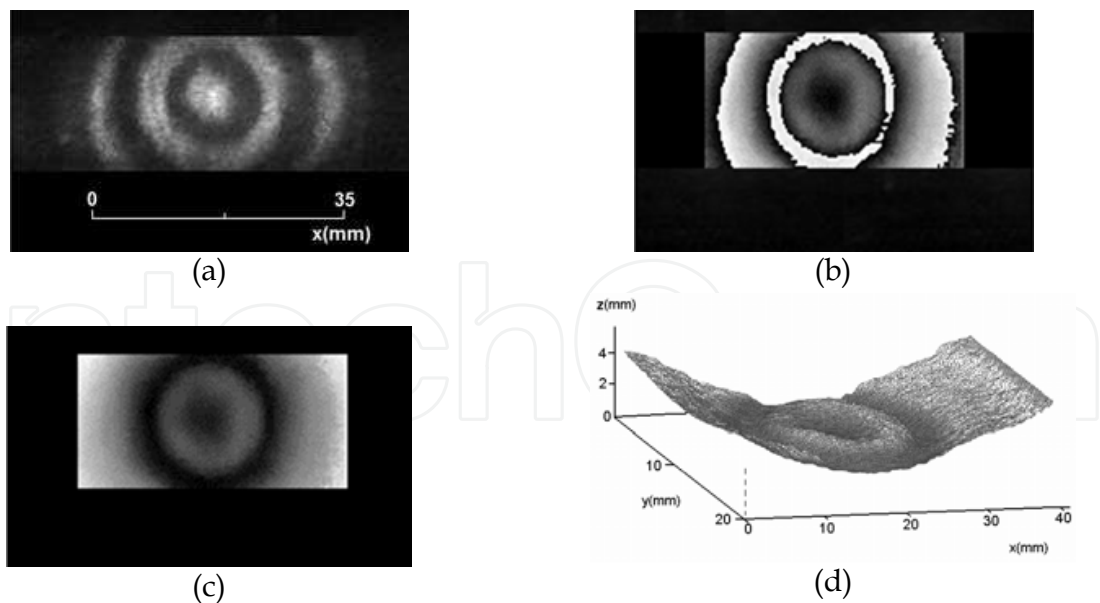


Fig. 5. Profilometric analysis of a still loudspeaker. (a) - Interferogram; (b) - phase map; (c) - unwrapped phase pattern and (d) - three-dimensional plot (Barbosa et al, 2005).

Since both the beam which illuminates the object surface and the beam scattered by it propagate in nearly opposite directions, the planes of constant elevation are nearly perpendicular to both beams and the contour interval (i.e., the distance between two

adjacent planes of constant elevation) is thus  $\Delta z \cong \lambda_s/2$ . Figure 5a shows the holographic image of a partially illuminated still loudspeaker for  $N = 3$ . The spatial frequency of the contour fringes is due to the laser free spectral range of  $\Delta\nu = 53$  GHz, corresponding to  $\Delta z = 2.66$  mm, for a central emission wavelength of 670 nm. In the four-stepping process the translation stage was displaced by  $\Delta z/4 = 0.66$  mm, resulting the phase map shown in figure 5b. The unwrapped phase pattern obtained through the cellular-automata method is shown in figure 5c, while the three-dimensional reconstruction of the plate is depicted in figure 5d, with an enlarged scale in the z-direction.

### 3.4 Methods for enhancing the measurement sensitivity

It has been mentioned in the previous sections that the contour interval  $\Delta z$  equals the laser resonator length  $L$  when the illuminating and the scattered beams propagate in opposite directions. If this property on the one hand make the diode lasers quite suitable in the profilometry of objects with several millimetres to few centimetres of size, on the other hand it may be a limitation remarkably in the measurement of nearly flat, low-derivative surfaces, which require smaller  $\Delta z$  values in order to minimize the measurement noise. The next sections present the most employed methods to overcome this limitation and to obtain interferogram spatial frequencies which are higher than the ones usually obtained through a single multimode laser. Those procedures aim more accurate visual inspections and the decrease of the measurement noise.

#### 3.4.1 Recording with two phase-shifted reference beams

Holographic processes using lasers emitting more than two longitudinal modes results in bright interference fringes which are narrower than the  $\cos^2$ -fringes obtained in two-wavelength techniques. One can take advantage from this property in order to obtain holographic images by using optical setups with two properly shifted reference beams. In multi-wavelength holographic processes generated by more than two wavelengths ( $N > 2$  in equation 11), the resulting bright fringes are sufficiently narrow to allow the superposition of two interferograms and generate a third one. Let us consider the incidence of two reference beams 1 and 2 with intensities  $I_{R1}$  and  $I_{R2}$ , such that  $I_{R1} = I_{R2} = I_R/2$ . The resulting holographic image of the object in this case is the incoherent sum of two interferograms, each one generated by the interference of the object wave with one of the reference waves. The intensity of the interferograms superposition can be written as (Barbosa et al, 2005)

$$I_D' = 4\eta_0 \{4 \cos^2[\Delta k_{eff}(\Gamma_S - \Gamma_{R1})/2] + 1\} I_R, \quad (15)$$

where  $\Delta k_{eff} \equiv 2\pi/\lambda_{eff}$  can be regarded as an effective wavelength interval and  $\lambda_{seff} = \lambda^2/(2\Delta\lambda) = \lambda_s/2$  is the effective synthetic wavelength. The fact that  $\lambda_{seff} = \lambda_s/2$  implies that the interferogram generated by the superposition of both fringe patterns has twice their spatial frequency. Figure 6a shows the intensity distribution of the interferogram generated by a single reference beam for  $N = 3$  laser modes as a function of the object coordinate  $\Gamma_S$  (taking  $\Gamma_R$  arbitrarily as zero) according to equation (11), while figure 16b shows the fringe pattern generated by two reference beams according to equation (15) with optical paths adjusted so that  $\Gamma_{R2} - \Gamma_{R1} = q\lambda_{seff}$ , ( $q = 1, 2, 3, \dots$ ). Both figures have the same  $\Gamma_S$ -scale, showing that the second interferogram has twice the spatial frequency than that of the

first one. Consequently, the profilometry sensitivity is twice enhanced when the optical paths of the two reference beams are properly adjusted. Figure 6c shows the holographic image the loudspeaker studied in section 3.3.1 with two reference beams. The higher spatial frequency of the resulting interferograms allows for a more detailed surface visualisation, leading to a more accurate qualitative analysis.

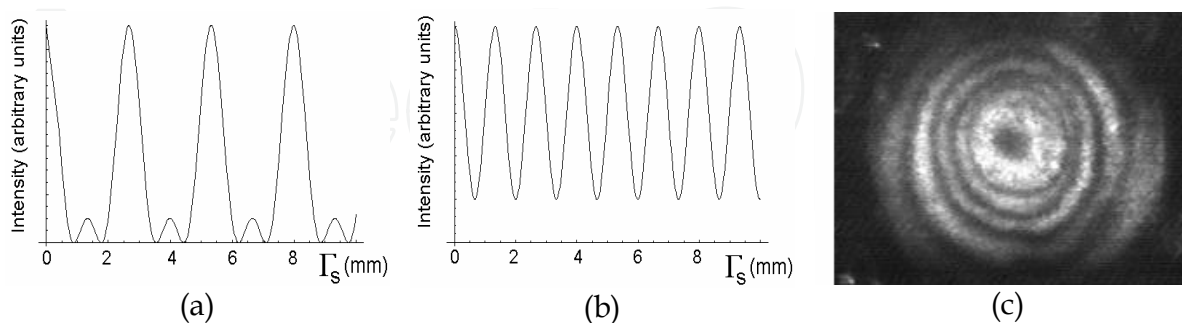


Fig. 6. - Interferogram intensity distribution as a function of  $\Gamma_S$  for holographic recording with (a) - one reference beam and (b) - two reference beams; (c) - Holographic image of the loudspeaker generated by a two-reference beam setup (Barbosa et al, 2005)

### 3.4.2 Laser mode selection by extra-cavity Fabry-Perot etalons

This section shows how the interferogram spatial frequency can be increased by placing an extracavity Fabry-Perot étalon (FBE) at the laser output. If the FBE is placed at the laser output and conveniently aligned a small fraction of the output beam is reflected back into the laser diode. Only the modes which are re-injected will be amplified while the oscillation of the others will vanish. This increases the effective free spectral range of the emission, thus raising the spatial frequency of the contour interferogram. After positioning the FBE at the laser output the synthetic wavelength  $\Lambda_S$  upon mode selection is obtained as (Barbosa et al, 2007):

$$\Lambda_S = \frac{1}{m} \frac{\lambda^2}{\Delta\lambda} = \frac{\lambda_s}{m}, \quad (16)$$

Equation (16) shows that, by conveniently adjusting the FBE spacing, the synthetic wavelength  $\Lambda_S$  achieved by mode selection can be progressively scaled to smaller values. This scaling is limited by the number of longitudinal modes of the laser emission. If  $m = 1$ , all modes are reflected back into the laser resonator, so there is no mode selection and thus no changes in the interferogram are observed. If  $m > 1$  only some modes are reinforced, and the resulting free spectral range of the laser illuminating the holographic setup increases, thus increasing the interferogram spatial frequency and enhancing whether the measurement sensitivity or the profilometry resolution.

Figure 7a shows the holographic image of a flat tilted plate with a multimode diode laser without FBE. The holographic medium is a BTO crystal cut in the electrooptic transverse configuration. In this case,  $\Lambda_S = \lambda_s = 5.30$  mm and  $\Delta z = 2.65$  mm. Figure 7b compares the  $z$ -coordinate of a cross section of the plate reconstructed from the unwrapped with the expected profile of the plate. Figure 7c shows the contour fringe pattern of the same plate, at the same position, with the FBE adjusted for  $m = 3$ , leading to a synthetic wavelength

$\Lambda_S = 1.76$  mm and a contour interval  $\Delta z = 0.88$  mm, while figure 7d shows the resulting intensity profile of the same cross section of figure 7b.

By comparing figures 7b and 7d one comes to the conclusion that smaller contour intervals provide less noisy measurements as expected. The object profile of figure 7d presents smaller rms deviations from the expected plate shape if compared to the curve of figure obtained without mode selection. For both cases, the measurement fluctuations are  $\sim 1/20$ th of a fringe.

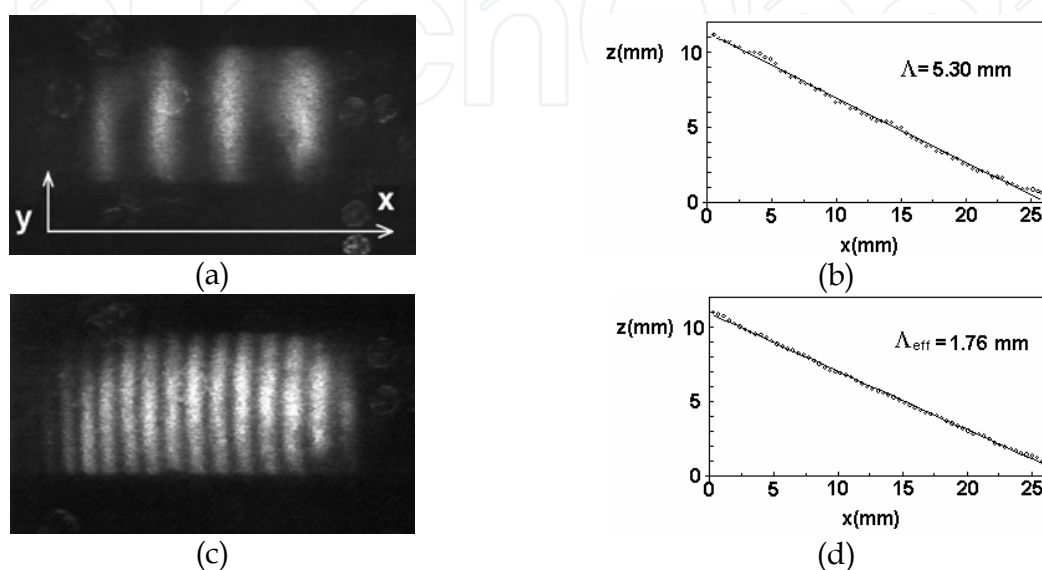


Fig. 7. Profilometry of a tilted plate. (a) - Interferogram for  $\lambda_S = 5.30$  mm and  $\Delta z = 2.65$  mm; (b) - corresponding profile; (c) - Interferogram for  $\lambda_S = 1.76$  mm and  $\Delta z = 0.88$  mm; (d) - profile of the same section (Barbosa et al, 2007).

#### 4. Two-laser holography in volume media

In this section the theory and the experiments concerning the employ of two tunable lasers in holographic wavefront reconstruction are exposed and discussed. In order to obtain smaller values of the contour interval  $\Delta z$  and improve the measurement sensitivity, the central wavelengths of both lasers are tuned allowing the simultaneous illumination of the object with two slightly different wavelengths thus providing a very wide range of  $\Delta z$  values. From the typical values of contour intervals in the order of few millimetres obtained through single-multimode lasers, experiments using two-laser schemes can decrease these values down to  $40 \mu\text{m}$ . Since the fringe evaluation techniques exposed in section 3.3.1 achieve measurement precisions up to  $1/100$  of a fringe in low optical noise experiments, the two-laser holographic processes represent a great sensitivity and precision improvement in wavefront reconstruction through heterodyne holography.

The two-laser optical setup using also a BTO crystal as storage medium shown in figure 8 is essentially the same of that shown in figure 4, except by the arrangement at the beam splitter BS which couples the beams coming from lasers 1 and 2. The arm of the interferometer containing the transmitted reference beam is sent to a spectrum analyzer with a 1200-lines/mm diffraction grating for wavelength monitoring. Mirror M4 can be translated and tilted in order to spatially couple the beams originated from both lasers.

Consider that the diode lasers emit at the wavelengths  $\lambda_1$  and  $\lambda_2$  such that  $|\lambda_1 - \lambda_2| \ll \lambda_1$ . The following analysis takes into account the influence of the lasers detune and the misalignment of the beams on the generation of interference contour fringes on the object image. If  $\Gamma_{S1,2}$  and  $\Gamma_{R1,2}$  are respectively the optical paths of the object and the reference beams with wavelength  $\lambda_{1,2}$  from the coupling beam splitter to the crystal, the waves impinging the BTO crystal can then be written as (Barbosa & Carvalho, 2007)

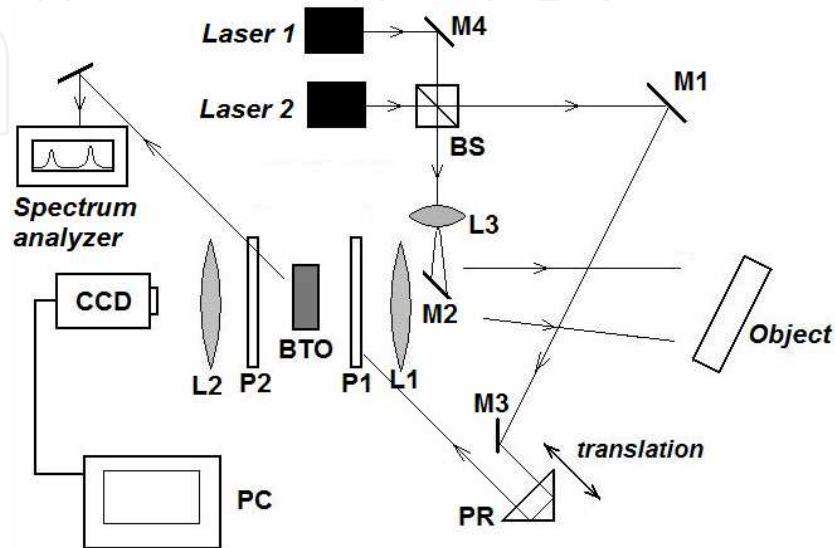


Fig. 8. Two-laser holographic interferometer

$$\begin{aligned} R &= R_0 \left( e^{i(k_1 \Gamma_{R1} + \phi_1)} + e^{i(k_2 \Gamma_{R2} + \phi_2)} \right) \\ S &= S_0 \left( e^{i(k_1 \Gamma_{S1} + \phi_1)} + e^{i(k_2 \Gamma_{S2} + \phi_2)} \right) \end{aligned} \quad (17)$$

where  $k_{1,2} = 2\pi/\lambda_{1,2}$ . The distinction between  $\Gamma_{S(R)1}$  and  $\Gamma_{S(R)2}$  takes into account an eventual (and sometimes quite useful) beam misalignment at the beam splitter output. Due to the interaction of waves with two different wavelengths, there are two recorded holograms in the crystal. According to equations 10a-c, the diffraction of reference wave 1 by both holograms provides the holographic reconstruction of the object wavefront given by

$$E_{D1} = \sqrt{\eta_0} R_0 \left[ e^{ik_1 \Gamma_{S1}} + \chi_{1,2} e^{i(k_1 \Gamma_{R1} + k_2 \Gamma_{S2} - k_2 \Gamma_{R2})} \right] \quad (18)$$

The holographic reconstruction of the object occurs correspondingly for the diffraction of reference wave 2, resulting in the wave amplitude  $E_{D2}$ :

$$E_{D2} = \sqrt{\eta_0} R_0 \left[ e^{ik_2 \Gamma_{S2}} + \chi_{1,2} e^{i(k_2 \Gamma_{R2} + k_1 \Gamma_{S1} - k_1 \Gamma_{R1})} \right] \quad (19)$$

where  $\chi_{1,2} = \sin \xi_{1,2} / \xi_{1,2}$ ,  $\xi_{1,2}$  being given by (Kogelnik, 1969)

$$\xi_{1,2} = 2\pi l_0 \sin \gamma \left[ \frac{\Delta \alpha}{\sqrt{\lambda_1 \lambda_2}} + n_0 \tan \gamma \frac{\Delta \lambda}{\lambda_1 \lambda_2} \right] \quad (20)$$

The angle  $\Delta\alpha$  accounts for the misalignment between the beams at the BS output and  $\Delta\lambda \equiv \lambda_1 - \lambda_2$ . In single multimode lasers,  $\Delta\lambda$  is the wavelength gap between two adjacent modes.  $\Delta\alpha$  is small enough to allow the superposition of the waves as they propagate from the BS to the holographic medium. In equations (18) and (19) the phases  $\phi_1$  and  $\phi_2$  at the lasers output were set arbitrarily to zero.

Both waves  $E_{D1}$  and  $E_{D2}$  are incoherent and combine at the crystal output as a sum of their intensities, thus providing the intensity of the holographic object image:

$$I_D \propto |E_{D1}|^2 + |E_{D2}|^2 \propto R_0^2 \eta_0 \left[ 1 + \chi^2 + 2|\chi| \cos(k_1\Gamma_{S1} - k_1\Gamma_{R1} - k_2\Gamma_{S2} + k_2\Gamma_{R2}) \right] \quad (21)$$

$$= R_0^2 \eta_0 (1 + \chi^2) \left[ 1 + V \cos(k_1\Gamma_{S1} - k_1\Gamma_{R1} - k_2\Gamma_{S2} + k_2\Gamma_{R2}) \right]$$

where  $V \equiv 2|\chi| / (\chi^2 + 1)$  is the interferogram visibility. Notice that since the output power is the same for both lasers,  $V$  refers only to the Bragg regime degree. By analyzing the phase in the sinusoidal term of equation (21), one retrieves information about the object surface, the position of the constant elevation planes and their relative distances as well as the interferogram localization.

#### 4.1 Interferogram positioning and distance between planes

Consider the incidence of the collimated illuminating beam onto the analyzed surface impinging points A and B as shown in figure 9. The angle between the incident beam and the normal direction with respect to the photorefractive sample front face (plane  $xz$ ) is  $\alpha + \Delta\alpha$  for beam 1 and  $\alpha$  for beam 2. The phase difference  $\phi$  between two points A and B on the object surface is obtained with the help of equation (21) :

$$\phi = k_1\Gamma_{S1B} - k_2\Gamma_{S2B} - k_1\Gamma_{S1A} + k_2\Gamma_{S2A}, \quad (22)$$

where  $\Gamma_{S1(2)A}$  and  $\Gamma_{S1(2)B}$  are the optical paths of the object beam at wavelength  $\lambda_{1(2)}$  through A and B, respectively. In the equation above, the influence of the beams misalignment in the reference-beam arm on the fringe generation can be considered negligible. According to figure 9, the phases of equation (22) can be explicitly written as a function of the unit propagation vectors of the illuminating and the scattered beams  $\hat{k}_1$ ,  $\hat{k}_2$  and  $\hat{k}$  as  $\Gamma_{1SA} = \hat{k}_1 \cdot \vec{r}_{1A} + \hat{k} \cdot \vec{r}_A$ ,  $\Gamma_{2SA} = \hat{k}_2 \cdot \vec{r}_{2A} + \hat{k} \cdot \vec{r}_A$ ,  $\Gamma_{1SB} = \hat{k}_1 \cdot \vec{r}_{1B} + \hat{k} \cdot \vec{r}_B$  and  $\Gamma_{2SB} = \hat{k}_2 \cdot \vec{r}_{2B} + \hat{k} \cdot \vec{r}_B$ .

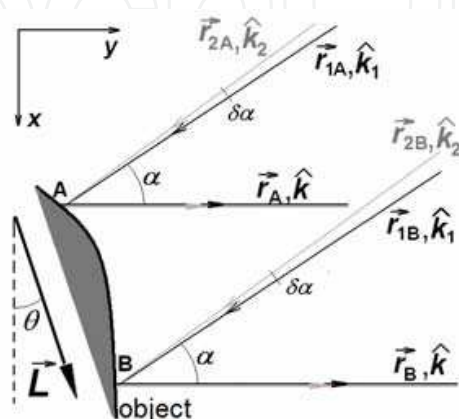


Fig. 9. Incidence of the waves onto the surface.

Vectors  $\vec{r}_{1A(B)}$ ,  $\vec{r}_{2A(B)}$  represent the displacement of the waves with wavelengths  $\lambda_1$  and  $\lambda_2$ , respectively, through point A (B), while  $\vec{r}_A$  and  $\vec{r}_B$  are the displacement vectors from points A and B to the BTO crystal front face. Vector  $\vec{L}$  is the position vector of point B with respect to A. By examining figure 9 one obtains the relations  $\hat{k}_1 \cdot (\vec{r}_{1A} - \vec{r}_{1B}) = \hat{k}_1 \cdot \vec{L}$ ,  $\hat{k}_2 \cdot (\vec{r}_{2A} - \vec{r}_{2B}) = \hat{k}_2 \cdot \vec{L}$  and  $\hat{k} \cdot (\vec{r}_B - \vec{r}_A) = \hat{k} \cdot \vec{L}$ . From equation (22) and the relations above  $\varphi$  is written as (Barbosa, 2010)

$$\varphi = 2\pi \left( \frac{\hat{k}_1}{\lambda_1} - \frac{\hat{k}_2}{\lambda_2} - \frac{\hat{k}}{\lambda_s} \right) \cdot \vec{L} \quad (23)$$

where  $\lambda_s \equiv \lambda_1 \lambda_2 / (\lambda_2 - \lambda_1)$  is the synthetic wavelength for the two-laser holographic process. Depending on the lasers tuning, the synthetic wavelength can be whether positive or negative. According also to figure 9, the vectors in equation (23) can be written as a function of  $\alpha$  and  $\theta$  as  $\hat{k}_1 = (\sin \alpha, -\cos \alpha)$ ,  $\hat{k}_2 = (\sin(\alpha + \delta\alpha), -\cos(\alpha + \delta\alpha))$ ,  $\hat{k} = (0, 1)$  and  $\vec{L} = L(\sin \theta, \cos \theta)$ .

The phase obtained in equation (23) describes the generation of contour fringes due to two-laser holography. With the help of this equation it is also possible to determine important parameters of the surface measurement, like the direction of the constant elevation planes, the distance between two adjacent planes and the position of the contour interferogram with respect to the object surface.

If points A and B lay on the same plane of constant elevation (i.e., on the same bright/dark fringe), thus  $\varphi = 0$  and from equation (23) one obtains the direction of the elevation planes given by angle  $\theta$ :

$$\text{tg}\theta = \frac{\sin \alpha - \Im \cos \alpha}{2 \cos^2 \left( \frac{\alpha}{2} \right) + \Im \sin \alpha}, \quad (24)$$

where  $\Im \equiv \lambda_s \Delta\alpha / \lambda_2$ . Equation (24) shows that the direction of the planes of constant elevation with respect to the  $x$ -axis depend not only on the illumination angle, but also on the lasers detune and the misalignment  $\Delta\alpha$ . Notice that, when  $\Delta\alpha = 0$ , thus  $\theta = \alpha/2$ , i.e. the constant elevation planes are perpendicular to the bisector formed by the illuminating beam and the beam scattered by the object, a well-known result in conventional two-colour holography and used in the previous sections. As  $\Delta\alpha$  increases, however, the planes rotate and may significantly change the contour interference pattern, remarkably for larger synthetic wavelengths.

It should be also noticed that the wavelengths detune and the misalignment  $\Delta\alpha$  cannot be set at arbitrary values. As exposed in section 2, the limitations imposed by the Bragg regime must be necessarily considered and thus there must be a trade-off between all the parameters in order to obtain acceptable interferogram visibilities. Concerning the Bragg regime in the recording and readout, the terms  $\Delta\alpha$  and  $\lambda_2 - \lambda_1$  are related to each other according to equation (20). The interferogram maximal visibility  $V_{\max} = 1$  obtained in perfect Bragg processes is achieved for  $\xi = 0$  and  $\chi = 1$ . This tolerance for slight off-Bragg regimes may result in higher spatial frequency interferograms and make the conditions for beam alignment less severe. The term  $\Im$  appears recurrently throughout this analysis and will deserve special attention, since it is closely related to the Bragg condition.

With the help of the first-order expansion  $\chi = \sin \xi / \xi \cong 1 - \xi^2/6$ ,  $\mathfrak{S}$  can be written as

$$\mathfrak{S} \cong \frac{\sqrt{6(1-\chi)}}{2\pi l_0 \sin \gamma} \lambda_s - \frac{\tan \gamma}{n_0} \quad (25)$$

where  $(\lambda_1/\lambda_2)^{1/2}$  was considered to be  $\approx 1$ . The term  $\mathfrak{S}$  determines how the lasers can be tuned and how the beams can be aligned in order to combine desired values of contour intervals without significantly decreasing the interferogram visibility.

The distance between two consecutive planes of constant elevation can be obtained with the help of equation (23). Let us call  $\vec{R}$  as the *sensitivity vector*, representing the distance between two consecutive planes. Since the phase difference between them is  $\varphi = 2\pi$  rad, one obtains the relation

$$\left( \frac{\hat{k}_1}{\lambda_1} - \frac{\hat{k}_2}{\lambda_2} - \frac{\hat{k}}{\lambda_s} \right) \cdot \vec{R} = 1 \quad (26)$$

Since  $\vec{R} \perp \vec{L}$ , from equation (23) the modulus of  $\vec{R}$  is obtained as

$$R = \left| \frac{\lambda_s}{\mathfrak{S} \sin(\theta - \alpha) - 2 \cos\left(\frac{\alpha}{2}\right) \cos\left(\theta - \frac{\alpha}{2}\right)} \right| \quad (27)$$

In order to illustrate the influence of the lasers wavelengths on the position of the constant elevation planes, let us analyze the experimental situation in which the wavelengths  $\lambda_1$  and  $\lambda_2$  of lasers 1 and 2 behave in such a way that  $\lambda_1 > \lambda_2$  is their whole tunability ranges. The aim of this analysis is to study the alignment requirements through which the constant elevation planes are parallel to the  $x$ -axis in figure 9, what is equivalent to say that the planes are parallel to the front face of the holographic medium. This configuration is particularly interesting in the study of surface geometries which present symmetry with respect to the  $y$ -axis, e.g. spherical or cylindrical surfaces, since the qualitative analysis may become much more intuitive.

Since  $\lambda_1 > \lambda_2$ , one gets  $\lambda_s < 0$  for any tuning configuration. Hence, from the definition of  $\mathfrak{S}$  one concludes that equation (25) is only fulfilled if  $\Delta\alpha \geq 0$ , and consequently  $\mathfrak{S} \leq 0$ . This imposes limitations to the setup geometry.

The requirement that the planes of constant elevation must be parallel to the  $x$ -axis and perpendicular to the  $y$ -axis is achieved for  $\theta = 0$ , or  $\vec{L}$  perpendicular to the  $yz$ -plane. This is equivalent to say that vector  $\Delta\hat{k} = \hat{k}_1/\lambda_1 - \hat{k}_2/\lambda_2$  must be parallel to the  $y$ -axis. From equation (24) this requirement is fulfilled when

$$\mathfrak{S} = \tan \alpha \quad (28)$$

In the illumination scheme of figure 10a the desired plane direction cannot be achieved because in this case  $\alpha > 0$ , which is in disagreement with equation (28). Notice that vector  $\Delta\hat{k} (\perp \vec{L})$  cannot be made perpendicular to the  $y$ -axis, unless  $\lambda_2 > \lambda_1$ , which is impossible to achieve in those experimental conditions. Figure 10b shows the contour interferogram on a holographic image of a spherical surface generated through this illumination scheme with a positive illumination angle and a negative synthetic wavelength. The excentric,

elliptical-like contour fringes clearly evidence that the interferogram was a result of the intersection of the surface with elevation planes tilted with respect to  $x$ -axis ( $\theta \neq 0$ ). This interferogram asymmetry cannot be removed upon laser tuning or further beam alignment unless the fringe visibility strongly decreases. In these figures,  $\lambda_s = -480 \mu\text{m}$ .

On the other hand, in the arrangement of figure 10c the illumination angle was inverted with respect to the  $y$ -axis, while the relative angular positions of vectors  $\hat{k}_1$  and  $\hat{k}_2$  remained unchanged. In this second case it becomes clear that for certain values of the wavelengths the vector  $\Delta\hat{k}$  can be made parallel to the  $y$ -direction, as evidenced by the circular and concentric contour fringes of the same spherical surface shown in figure 10d.

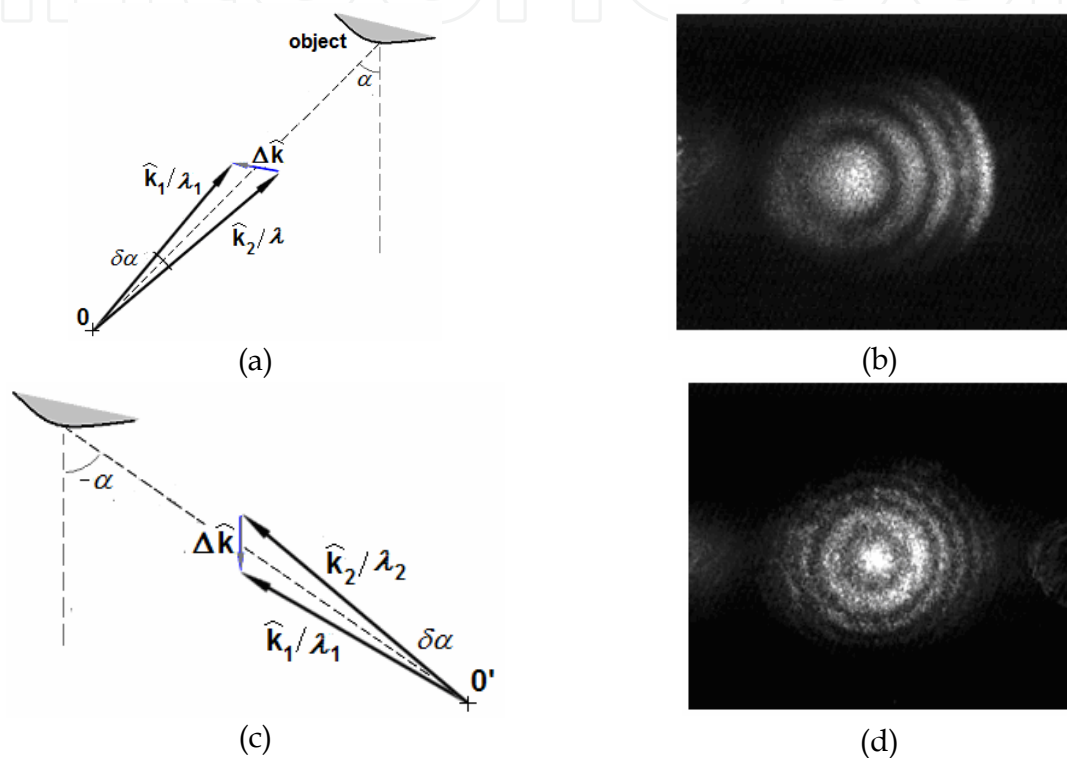


Fig. 10. (a) - Illumination scheme for  $\alpha > 0$  showing the vector  $\Delta\hat{k}$ ; (b) - contour interferogram of the surface obtained with positive  $\alpha$ ; (c) - illumination scheme for  $\alpha < 0$ ; (d) - resulting contour interferogram of the surface with circular concentric fringes (Barbosa, 2010).

#### 4.2 Interferogram localization

In this section, it is assumed that the interferogram is not formed at the object surface, but somewhere else near this region. Consider a point  $Q$  belonging to the region where the fringe pattern is formed; the total optical wave at  $Q$  is the contribution from the waves scattered by the points at the vicinity of a point  $P$  which in turn lays on the surface. The region surrounding  $P$  is the base of a cone with the apex at  $Q$  and whose area is directly proportional to the optical aperture of the imaging lens. The condition for fringe formation at point  $Q$  requires that the fringe visibility is a maximum, which implies that the phase variation at this point is a minimum. The interferogram intensity at a point  $P$  on the object can be attributed to its phase with respect to a point  $O$  on a reference constant elevation plane. Since points  $O$  and  $P$  define a vector  $\vec{H}$  parallel to the sensitivity vector, it is convenient to choose a new coordinate system with axes  $x'$  and  $y'$  perpendicular and

parallel to vector  $\vec{H}$ , respectively, as shown in figure 11. Hence, the contour fringe at  $Q$  with phase  $\delta$  is formed if  $\partial\delta/\partial x' = 0$  (Vest, 1979).

Considering points  $P$ ,  $O$  and  $Q$  in the new coordinate system as having coordinates  $(x', H)$ ,  $(x', 0)$  and  $(X', Y')$ , respectively, the phase at  $Q$  is determined analogously as in the previous section according to the scheme of figure 11:

$$\delta \cong 2\pi \left( \frac{\hat{k}_2}{\lambda_2} - \frac{\hat{k}_1}{\lambda_1} - \frac{\hat{k}_3}{\lambda_s} \right) \cdot \vec{H} \quad (29)$$

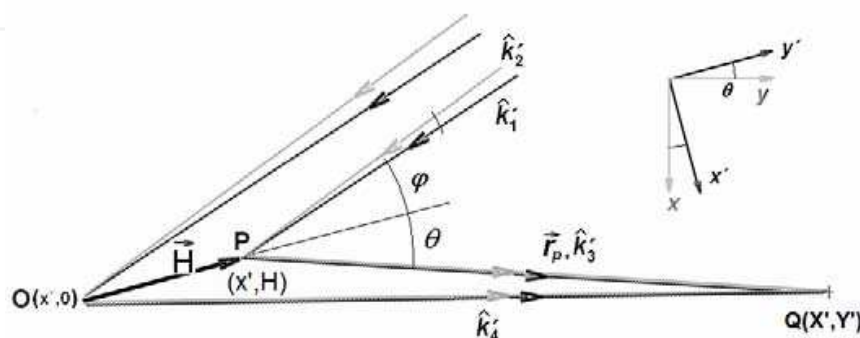


Fig. 11. Incident collimated beams and beams scattered by the surface at point  $P$ .

where  $\hat{k}_1$  and  $\hat{k}_2$  are the propagation vectors of the illuminating beams. Equation (29) was obtained considering a small incidence angle  $\alpha$  of the illuminating beam onto the object surface (as in the experimental setup) and the fact that  $\hat{k}_3 - \hat{k}_4$  and  $\vec{r}_p$  are nearly orthogonal.  $\hat{k}_3$  and  $\hat{k}_4$  are the propagation vectors of the scattered beams (see figure 11), and  $\vec{r}_p$  the position vector of  $P$  relatively to  $Q$ . According to figure 11 the position vector  $\vec{H}$  and the normalized propagation vectors are written as  $\vec{H} = (0, H)$ ,  $\hat{k}_1 = (\sin \alpha', -\cos \alpha')$ ,  $\hat{k}_2 = (\sin(\alpha' + \Delta\alpha), -\cos(\alpha' + \Delta\alpha))$  and  $\hat{k}_3 = (X' - x', Y' - H)\kappa^{-1}$ , where  $\kappa \equiv \sqrt{(X' - x')^2 + (Y' - H)^2}$ ,  $\varphi = \alpha - \theta$  and  $H = H(x')$ .

After some algebraic manipulation the position  $Y'$  where the fringe pattern is formed can be obtained from equation (29) as

$$Y' = \left\{ 1 + \frac{\frac{\sin 2\theta}{2} \left( \sin \theta \frac{\partial H}{\partial x'} - \cos \theta \right)}{\left[ 3 \sin(\alpha - \theta) + 2 \cos\left(\frac{\alpha}{2}\right) \cos\left(\theta - \frac{\alpha}{2}\right) \right] \frac{\partial H}{\partial x'}} \right\} H(x') \quad (30)$$

Equation (30) provides the relative position of the interferogram with respect to the object surface. When the expression in the brackets equals 1, then  $Y' = H(x')$ , and the fringe pattern occurs right on the object surface. As the expression in the brackets assumes values smaller than 1, the fringe pattern is formed behind the object; otherwise, the interferogram is formed between the object surface and the imaging lens. Equation (30) shows also that the slope  $\partial H/\partial x'$  of the studied surface and the illumination angle  $\alpha$  determine whether the fringes are formed behind or in front of the surface.

Since  $|\Im \sin(\alpha - \theta)| < 2 \cos(\alpha/2) \cos(\theta - \alpha/2)$  in typical experimental conditions, one notes also from equation (30) that the fringe pattern is formed behind the surface ( $Y' < H(x')$ ) for positive surface slopes ( $\partial H/\partial x' > 0$ ). Correspondingly, if  $\partial H/\partial x' < 0$ , one gets  $Y' > H(x')$ , and the interferogram is formed between the surface and the imaging lens.

The holographic images of the "V"-shaped surface constituted of two concurrent planes shown in figure 12 confirm those predictions, for  $\lambda_s = -420 \mu\text{m}$ ,  $\Delta\alpha = 2 \times 10^{-4}$  rad and  $\alpha = 5 \times 10^{-2}$  rad. The two halves of the surface present slopes of different signals. In figure 12a, while the interferogram on the left side with negative slope presents a good visibility, the fringe pattern on the right side with positive slope appears completely blurred. On the other hand, in figure 12b, when the interferogram of the right half of the surface is focused, the contour fringes of the left half cannot be visualized.

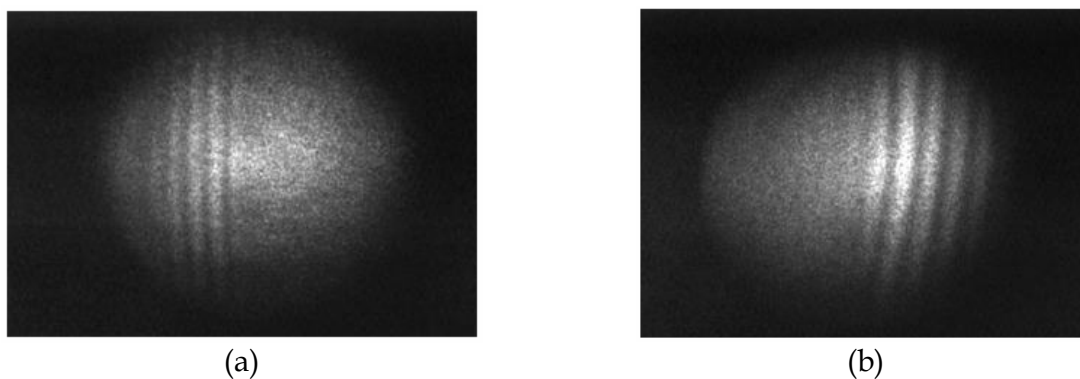


Fig. 12. Two-wavelength holographic imaging of the V-shaped surface by focusing the fringe pattern of (a) - the left half ( $x' > 0$  and  $\partial H/\partial x' < 0$ ) of the surface, and (b) - the right half of the surface ( $x' < 0$  and  $\partial H/\partial x' > 0$ ) (Barbosa, 2010)

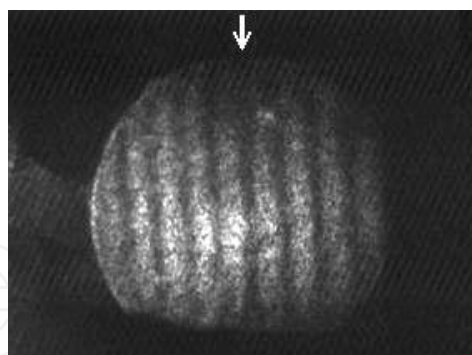


Fig. 13. Two-wavelength contour interferogram of the whole V-shaped surface for  $\theta = 0$ . The arrow shows the limit between the negative and the positive slope of the surface (Barbosa, 2010).

The limitation of focusing the whole contour interferogram of a surface with slopes of different signals can be overcome by adjusting the setup in order to set the direction of the constant elevation planes as  $\theta = 0$ . According to equations (30), in this case one gets  $Y' = H$ , and the fringe pattern is formed right on the surface, regardless its geometry. This configuration does enable and easier and more intuitive visual inspection of the surface shape. The contour interferogram of the same "V"-shaped object of Figure 12 was studied under the same value of  $\Im$ ; the illumination angle  $\alpha$  in turn was set at negative values in

order to obtain null values of  $\theta$ , according to equations (24) and (28). Figure 13 shows the resulting contour fringe pattern with the arrow indicating the edge position which separates the negative slope from the positive slope of the surface. As expected, the contour fringes pattern can be clearly visualized along both sides of the surface, regardless the aperture of the optical system.

## 5. Further applications

### 5.1 Holographic refractometry

Many refractometry methods and devices have been developed for material characterization. Refractometry is useful for identifying unknown liquid compounds, to evaluate their purity, or to determine the solute concentration in solutions by comparison with standard curves. Most of the techniques make use of purely geometrical optics phenomena like ray deviation or total internal reflection (McAlister et al, 1956). Interferometric (Santiago Neto et al, 2004), holographic (Gustafsson & Sebesta, 2004) and other methods combining ray optics with diffractive components (de Angelis et al, 1996) have been also presented. Multi-wavelength holography with photorefractive materials can be successfully employed for liquid and amorphous material characterization through refractometry. The principle of holographic refractometry is based on the measurement of fringe displacement generated by the variation on of the optical path inside the test cell containing the sample.

The optical setup for liquid characterization is shown in figure 14. In this setup a simple flat plate tilted with respect the holographic medium is the object, as accomplished in the experiments described in section 3. However, in this holographic refractometer the reference beam passes through a glass cell filled with the liquid with a moveable reflector inside. By translating the reflector, the optical path inside the liquid is changed, thus changing the optical path of the reference beam. According to equation (11), this shifts the parallel and straight contour fringes formed on the holographic image of the tilted plate. This can be described in more detail with the help of figure 14a, which shows the reference beam propagation through the test cell. Inside the glass cell and immersed in the liquid, the prism  $90^\circ$ -prism PR is used as a retro-reflector. If PR is translated by  $\Delta L$ , the optical path change into the reference beam is  $2n\Delta L$ . According to equation (11), this leads to the following expression for the refractive index:

$$n = \frac{\lambda_s p}{2\Delta L}, \quad (31)$$

where  $p$  is the number of running fringes across the object image. This experimental configuration features some important characteristics. The reduced rectangular cross section of the test cell requires relatively small amounts of liquid even for somewhat large optical paths of the reference beam; the small diameter of the collimated reference beam propagating through the liquid allows a high light intensity at the holographic medium in spite of moderate scattering and absorption losses in the liquid. This makes the requirements for flatness and thickness uniformity of the cell walls much less severe. Moreover, the scalableness of the measurement precision is other interesting property of this refractometer: several reflector configurations can be employed in order to enlarge the effective optical path of the reference beam through the liquid without significantly enlarging the liquid quantity.

The optical scheme designed for a compact and portable holographic refractometer prototype using a BTO crystal as the storage medium and a single multimode diode laser is depicted in figure 14b (Barbosa et al, 2010). The prism PR is supported by a mount from the top of the test cell, in a way that there is no mechanical contact between the PR mount and the cell walls. A 5- $\mu\text{m}$  resolution step motor and a translation stage move the reflector mount along the  $x$ -axis in a closed loop. The synthetic wavelength in this case was measured to be  $\lambda_s = 6.6280 \pm 0.0005$  mm and the test cell of this prototype permitted a maximum PR translation of  $\sim 70$  mm. Hence, when the test cell is empty and the PR suffers a complete translation, one observes the displacement of 21 contour fringes through a reference point on the object image. If the test cell is filled e.g. with pure water ( $n_{\text{water}}=1.3317$ ) then one counts 28 running fringes for nearly the same prism displacement, and so forth.

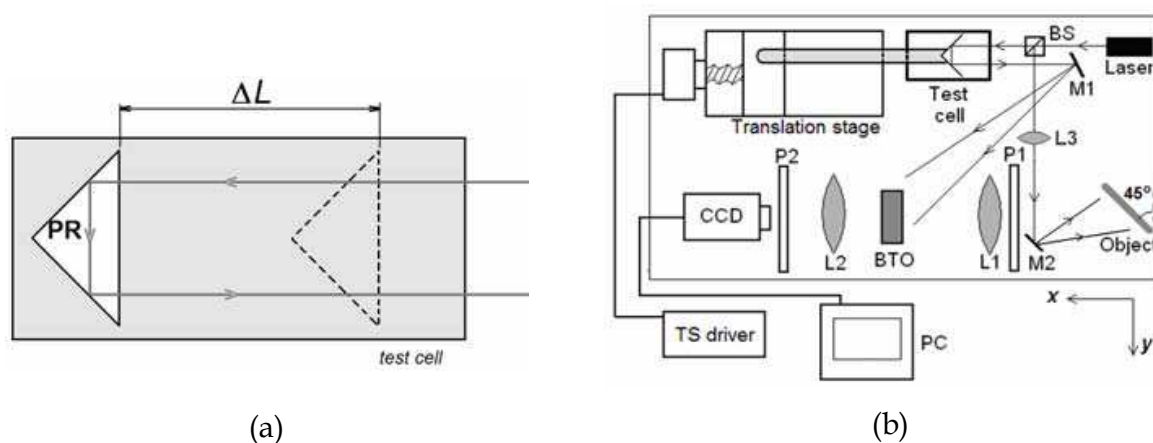


Fig. 14. (a) - 90°-prism retro reflector PR in test cell; (b) - Optical setup for the holographic refractometer : BTO,  $\text{Bi}_{12}\text{TiO}_{20}$  crystal; BS, beam splitter; M1 and M2, mirrors; P1 and P2, polarizers; L1 to L3, lenses; translation stage TS driver , CCD camera and PC computer for image acquisition (Barbosa et al, 2010).

The setup of figure 14b allows the use of a second laser for two-laser holographic recording measurements. The consequent generation of significantly smaller synthetic wavelengths in this case enables the use of much smaller liquid quantities without decreasing the measurement precision, which is a very desirable condition for the analysis of turbid liquids. As an example, the refractive index measurement of a sample of a highly scattering artificial melon juice is briefly described: taking into account scattering and absorption, the total loss on the reference beam due to the juice was 7.5 %, corresponding to a loss coefficient for red light of  $\approx 0.13$   $\text{cm}^{-1}$ , according to Beer's law. By properly tuning the lasers to obtain a wavelength difference of  $\lambda_1 - \lambda_2 = 0.56$  nm a synthetic wavelength of  $\lambda_s = 788.81 \pm 0.3$   $\mu\text{m}$  was generated. This  $\lambda_s$ -value was small enough to allow a fringe displacement of 18 fringes upon a translation of only (if compared to the 70-mm translation in the single multimode laser case)  $5.33 \pm 0.01$  mm of the prism reflector. According to equation (31), this successful measurement resulted in a refractive index of  $1.331 \pm 0.002$ .

## 5.2 Lens characterization

Several methods were proposed and developed for lens characterization, whether by purely geometrical optics or by interferometry. Moiré interferometry (Keren et al, 1988), diffraction gratings (de Angelis et al, 1997), lithographically recorded Fresnel Zone holograms (DeBoo

& Sasian, 2003) and digital holography (Anand & Chhaniwal, 2006), among other methods, were successfully applied for lens characterization. The common feature of those works is the fact that they are restricted to focal length measurement only. In order to provide a more complete study of the lens, this section is devoted to describe how the wavefront reconstruction methods exposed in section 3 and the refractometry techniques analyzed in the previous section can be combined in order to integrally characterize several types of spherical and toric lenses. For this reason, this technique of lens characterization is able to measure all their refractive and geometric parameters through two-laser holography. This is accomplished by reconstructing three wavefronts: the surfaces of both sides of the lens - which provides their radii of curvatures - and the shape of the wave that propagates through the lens, impinges a opaque and diffusely scattering plane surface and travels back again through the lens. This latter measured wavefront is used to determine the lens refractive index by adjusting the experimental data to the corresponding wavefront calculated through exact ray tracing. This calculation is performed as a function of the radii of curvature, the refractive index and the thickness of the lens.

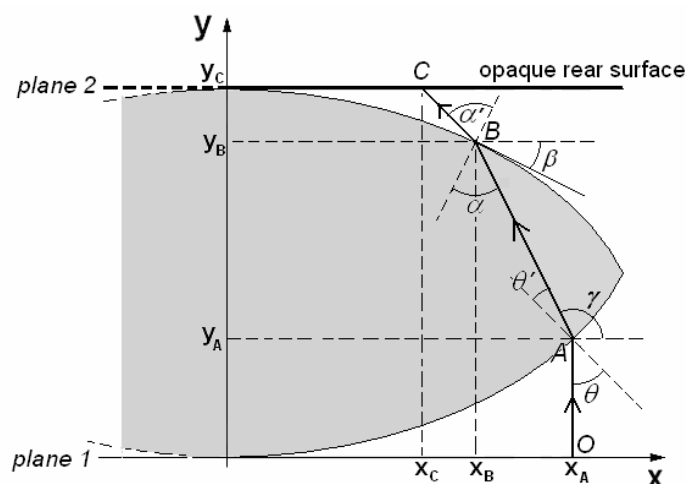


Fig. 15. Beam propagation through the spherical test lens

Figure 15 shows the scheme of the test lens with refractive index  $n$ , thickness  $t$  and radii of curvature  $R_F$  and  $R_R$  and the optical path of the incident beam. The beam travels from plane 1 to plane 2 and back to plane 1 through the spherical lens. The functions which describe the  $y$ -coordinate of the front and the rear surfaces in the  $xy$ -plane are given by  $y_F(x) = R_F - \sqrt{R_F^2 - x^2}$  and  $y_R(x) = t - R_R + \sqrt{R_R^2 - x^2}$ , respectively. In the experiments the opaque plane coinciding with plane 2 and perpendicular to the optical axis  $y$  was placed right behind the rear face of the test lens. The entrance pupil of the imaging lens is much smaller than the distance between the imaging lens and the test lens, thus, the total optical path  $\Gamma$  of the wave corresponds to twice the path  $\Gamma_{1 \rightarrow 2}$  introduced when the wave propagates from plane 1 to plane 2 only.

Since the input is a plane wave, the incident beam is parallel to the  $y$ -direction and impinges the front surface of the lens at point  $A$  of coordinates  $(x_A, y_A)$ . The total optical path of the light wave is then written as a function of the segments  $OA$ ,  $AB$  and  $BC$  according to

$$\Gamma_{1 \rightarrow 2} = (OA + nAB + BC) \tag{32}$$

where  $OA = y_A = R_F - (R_F^2 - x_A^2)^{1/2}$ . The calculation of  $AB$  and  $BC$  is lengthy but conceptually simple: by taking the derivative  $dy_F/dx$  for  $x = x_A$  the tangential and the normal curves to the front face are determined at point  $(x_A, y_A)$ . This provides angle  $\theta$  and through Snell's law angle  $\theta'$  (see figure 15) can be determined. The curve describing the beam propagating inside the lens can be written as a function of the angle  $\gamma = \theta - \theta' + \pi/2$  shown in figure 15 according to  $y_h(x) = x \tan \gamma - x_A \tan \gamma + y_A$ . The coordinates  $(x_B, y_B)$  of point  $B$  can be obtained from the relation  $y_h(x) = y_R(x)$ . Hence,  $AB$  is determined as  $AB = [(x_B - x_A)^2 + (y_B - y_A)^2]^{1/2}$ . By proceeding analogously at the lens rear surface one obtains straightforwardly the coordinates  $(x_C, y_C)$  of point  $C$ , providing the length  $BC$ , given by  $BC = [(x_C - x_B)^2 + (y_C - y_B)^2]^{1/2}$ . The total optical path of the beam in the  $xy$ -plane is thus given by

$$\Gamma_{1 \rightarrow 2} = y_A + n \left[ (x_B - x_A)^2 + (y_B - y_A)^2 \right]^{1/2} + \left[ (x_C - x_B)^2 + (y_C - y_B)^2 \right]^{1/2} \quad (33)$$

By comparing the experimentally reconstructed wavefront profiles with the optical path calculated in equation (33), the refractive index of the lens can be determined. The two-laser experimental apparatus is essentially the same as that of figure 8. The following figures refer as to the analysis of a 5.9-mm thick spherical lens made of BK7 glass with a diameter of 17 mm. In this technique the thickness is the only parameter obtained by conventional, i.e., non-optical means. In order to determine the radii of curvatures, each surface of this lens is covered by opaque films. The reconstructed wavefront after applying phase unwrapping procedures obtained with the contour interval  $\Delta z = 0.32$  mm is shown in figure 16a, while the averaged  $y$ -coordinate (circles) of the lens surface taken from figure 16a along radial directions and the fitting curve  $y(x) = R - (R^2 - x^2)^{1/2}$  (solid black curve) are shown in figure 16b. The radius of curvature of each surface is determined by fitting the experimental data with  $y(x)$ , providing the radius of curvatures  $R_F = 33.2$  mm. By performing analogously with the rear face, one obtains  $R_R = 32.9$  mm.

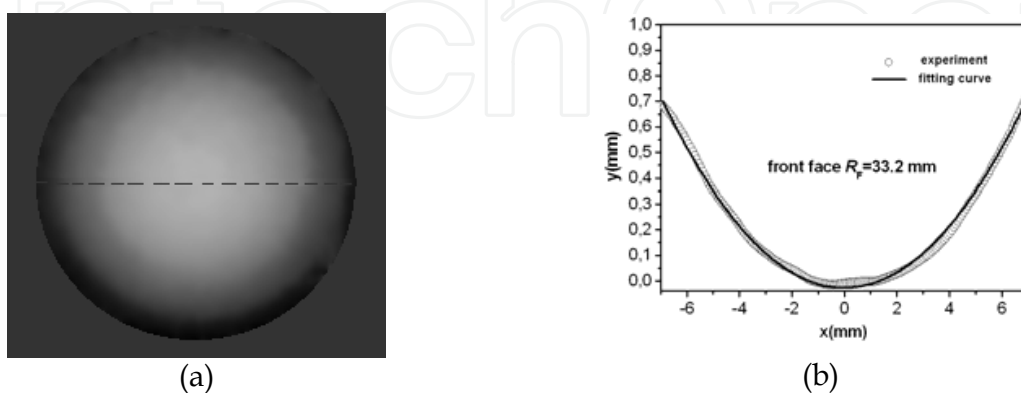


Fig. 16. Reconstruction of the front face of the lens; (a) - unwrapped phase; (b) -  $y$ -coordinate (circles) averaged along radial directions, and fitting curve (black curve) providing  $R_F = 33.2$  mm (Barbosa et al, 2009)

In order to measure the refractive index, the films are removed and the opaque surface is positioned behind the lens, so that the illuminating beam can propagate through the lens and hit the plate. The resulting contour fringe pattern of one of the four frames for  $\Delta z = 0.24$  mm is shown in figure 17a, while figure 17b shows the averaged  $y$ -coordinate of the reconstructed wavefront. The thick black line refers to the measured coordinates while the thin grey one is the fitting of the experimental data with the  $\Gamma$ -values given by equation (35). The best fitting in this case is obtained for  $n = 1.50 \pm 0.01$ . The measurement error defined as  $\delta(\%) = 100|n - n_E|/n_E$  was estimated to be  $\sim 0.7\%$ , considering the expected value for red light as  $n_E = 1.514$ .

Through the well-known formula

$$\frac{1}{f} = (n-1) \left[ \frac{1}{R_F} - \frac{1}{R_R} + \frac{t}{R_F R_R} \frac{(n-1)}{n} \right] \quad (34)$$

the focal length  $f$  can be determined. By using the experimental results  $R_F = 33.2$  mm,  $R_R = 32.9$  mm,  $t = 5.95$  mm and  $n = 1.50$ , the experimental focal length is determined to be 32.1 mm. The nominal focal length of the lens provided by the manufacturer is 32.4 mm, resulting in an experimental error of  $\sim 0.9\%$ .

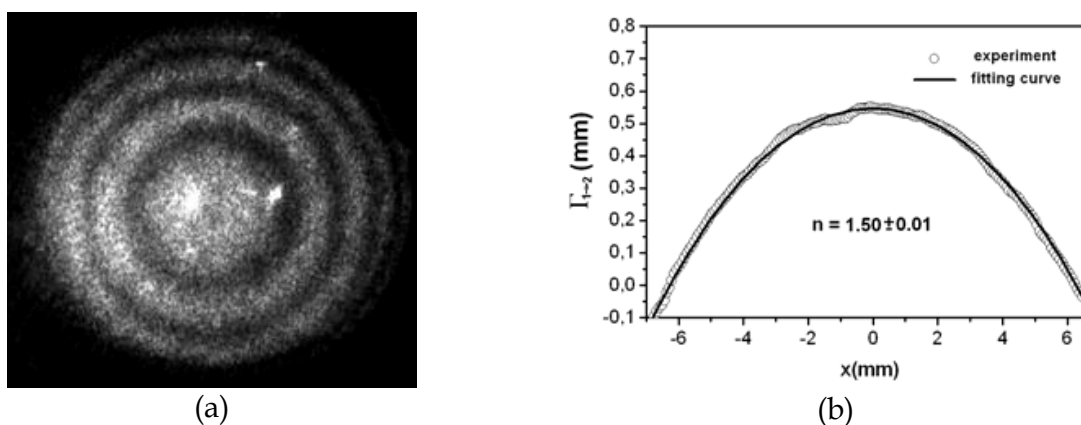


Fig. 17. (a) - Contour fringe pattern for  $\Delta z = 0.24$  mm when the illuminating beam traveled through the lens; (b) - averaged  $y$ -coordinate of the reconstructed wavefront providing  $n = 1.50 \pm 0.01$  (Barbosa et al, 2009).

## 6. Conclusion

Multi-wavelength holography has shown to be a powerful tool for optical metrology and wavefront reconstruction. Good visibility interferograms can be obtained in real-time processes, thus allowing faster and easier measurements with simple and compact optical setups. The profilometry techniques shown in this chapter presented the advantage of being nondestructive, thus allowing for the analysis of delicate surfaces, organic tissues or small objects, whose analysis by conventional, contacting means would not be viable. The whole-field character of holographic imaging provides also the additional advantage of the analysis of the whole surface, instead of lengthy point-by-point analyses.

Applications in refractometry and lensometry have shown the potentialities of multi-wavelength holography in these areas. The lens characterization method allows the

measurement of spherical, toric and other aspherical components with good precision and accuracy, while the holographic refractometry method allows the precise refractive index measurement of liquids with a measurable range which by far exceeds that of most of the commercial refractometres.

This work studied also the holographic recording and readout concerning the volume character of the photorefractive materials. Through this study, illumination procedures were successfully demonstrated in order to achieve good visibility interferograms. The anisotropic diffraction characteristics of the sillenite photorefractive materials, their high optical quality and high resolution capability are fundamental for the visualization of high-quality images.

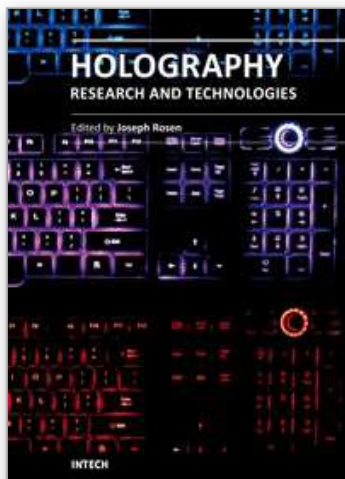
## 7. References

- Alam, M. S., Khoury, J. (2000). Photorefractive material based pattern recognition using fringe-adjusted correlation, *Proceedings of the SPIE Conference on Photorefractive Fiber and Crystal Devices: Materials, Optical Properties, and Applications*, pp. 14-17, ISBN 9780819437556, San Diego, California, 2000, SPIE, San Francisco
- Anand, A. , Chhaniwal, V. (2007). Measurement of parameters of simple lenses using digital holographic interferometry and a synthetic reference wave, *Appl. Optics* 46, 2007, 2022-2026, ISSN 1559-128X
- Barbosa, E.A., Muramatsu, M. (1997). Mapping of vibration amplitudes by time average holography in  $\text{Bi}_{12}\text{SiO}_{20}$  crystals, *Optics and Laser Technology* 29, June of 1997, 359-364, ISSN 0030-3992
- Barbosa, E.A. (2005). Holographic Imaging with multimode, large free spectral range lasers in photorefractive sillenite crystals, *Applied Physics B: Lasers and Optics* 80, 2005, 345-350, ISSN 0946-2171
- Barbosa E. A., Filho, A. A. V., Gesualdi, M. R. R., Curcio, B. G., Muramatsu, M., Soga, D. (2005). Single-exposure, photorefractive holographic surface contouring with multi-wavelength diode lasers, *Journal of the Optical Society of America A* 22, 2005, 2872-2879, ISSN 1084-7529.
- Barbosa, E. A., Lima, E. A., Gesualdi, M. R. R., M. Muramatsu (2007). Enhanced multi-wavelength holographic profilometry by laser mode selection, *Optical Engineering* 46, 2007, 075601-075607, ISSN 0091-3286
- Barbosa, E. A., Carvalho, J. F. (2007). Surface analysis by two-diode laser photorefractive holography, *Applied Physics B: Lasers and Optics* 87, 2007, 417-423, ISSN 0946-2171
- Barbosa, E. A, de Sousa, C. B. F., Maffei, W. M. (2009). Measurement of low-derivative surface lenses by two-laser holography with  $\text{Bi}_{12}\text{TiO}_{20}$  crystals, *Applied Optics* 48, 27, 2009, 5114-5120, ISSN 1559-128X
- Barbosa, E.A. (2010). Positioning and localization of two-wavelength interferograms for wavefront reconstruction with volume holographic media, *Optics Express* 18, 9, April 2010, 8743-8758, ISSN 1094-4087
- Barbosa, E.A., Silva, D. M., Preto, A. O., Verzini, R. (2010). Design, construction and performance of a real-time holographic refractometry setup for liquid analysis, accepted for publication in *Review of Scientific Instruments*, 2010.
- Chang, C., Chen T.C., Hon-Fai Yau, Ye P.X., Self-pumped and mutually pumped phase conjugation using pentagon-shaped  $\text{BaTiO}_3$  crystal, *Optical Materials* 18 (2001) 143-145, ISSN 0925-3467

- Chuang E., Psaltis D. (1997). Storage of 1000 holograms with use of a dual-wavelength method, *Applied Optics* 36 (1997) 8445-8454, ISSN 1559-128X
- De Angelis, M., de Nicola, S., Ferraro, P., Finizio, A., Pierattini, G. (1996), A reflective grating interferometer for measuring refractive index of liquids, *Optics Communications* 5, 1996, 761-765, ISSN 0030-4018
- De Angelis, S. De Nicola, P. Ferraro, A. Finizio, G. Pierattini (1997). A new approach to high accuracy measurement of the focal lengths of lenses using digital Fourier transform, *Optics Communications*, 136, 1997, 370-374, ISSN 0030-4018
- DeBoo, B., Sasian J. (2003). Precise Focal-Length Measurement Technique with a Reflective Fresnel-Zone Hologram, *Appl. Optics* 42 (2003) 3903-3909, ISSN 1559-128X
- Frejlich, J., Garcia, P. M. (2000). Advances in real-time holographic interferometry for the measurement of vibrations and deformations, *Optics and Lasers in Engineering* 32, December 2000, 515-527, ISSN 0143-8166
- Frejlich, J. (2006). Photorefractive Materials: Fundamental Concepts, Holographic Recording and Materials Characterization, Wiley, ISBN 9780471748663, New York
- Georges, M.P., Scaufaire, V.S., Lemaire, P.C. (2001). Compact and portable holographic camera using photorefractive crystals: Application in various metrological problems, *Appl. Phys. B: Lasers and Optics* 72 (2001) 761-765, ISSN 0946-2171
- Ghiglia, D. C., Mastin, G.A., Romero, L. A. (1987). Cellular-automata method for phase unwrapping, *Journal of the Optical Society of America A*, 1987, 210-219, ISSN 1084-7529.
- Gustafsson, M., Sebesta, M. (2004). Refractometry of Microscopic Objects with Digital Holography, *Applied Optics* 43, 25, 2004, 4796 - 4801, ISSN 1559-128X
- Gutmann, B., Weber, H. (1999). Phase Unwrapping with the Branch-Cut Method: Clustering of Discontinuity Sources and Reverse Simulated Annealing, *Applied Optics* 38, 26, 1999, 5577-5593, ISSN 1559-128X
- Hecht, E. (1987). *Optics*, 2<sup>nd</sup> Ed. Addison-Wesley, ISBN 020111609X, New York
- Kamshilin, A. A., Petrov, M. P. (1985). Continuous reconstruction of holographic interferograms through anisotropic diffraction in photorefractive crystals, *Optics Communications* 53, October 1984, 23-26, ISSN 0030-4018
- Keren, E., Kreske K. M., Kafri, O. (1988). Universal Method for determining the focal length of optical systems by moiré deflectometry, *Appl. Optics* 27, 1988, 1383-1385, ISSN 1559-128X
- Koehler, W. (1998), *Solid State Lasers Engineering*, Springer Verlag, ISBN 0-387-53756-2, Berlin
- Kogelnik, H. (1969). Coupled Wave Theory for Thick Hologram Gratings, *Bell Systems Technical Journal* 48, 9, November 1969, 2909-2947, ISSN 1538-7305
- Kuchel, F.M., Tiziani, H.J. (1981). Real-time contour holography using BSO crystals, *Optics Communications* 38, 1981, 17-21, ISSN 0030-4018
- Kukhtarev, N., Chen, B. S., Venkateswarlu, P. (1993). Reflection holographic gratings in [111] cut Bi<sub>12</sub>TiO<sub>20</sub> crystal for real time interferometry, *Optics Communications* 104, December of 1993, 23-28, ISSN 0030-4018
- Mallick, S., Rouède, D. (1987). Influence of the polarization direction on two beam coupling on photorefractive Bi<sub>12</sub>SiO<sub>20</sub>: Diffusion regime, *Applied Physics B: Lasers and Optics* 43, 1987 239-245, ISSN 0946-2171

- Millerd, J.E., Brock, N.J. (1997) . Holographic profilometry with a rhodium-doped barium titanate crystal and a diode laser, *Applied Optics* 36, 1997, 2427-2431, ISSN 1559-128X
- Pedrini, G., Fröning, P., Tiziani, H. J., Santoyo, F. M. (1999). Shape measurement of microscopic structures using digital holograms, *Optics Communications* 164 (1999) 257-268, ISSN 0030-4018
- Poon, T.-C, Banerjee P. P. (2001), *Contemporary Optical Image Processing With Matlab* , Elsevier Science ISBN-10: 0080437885, New York.
- Santiago Neto, R. B., de Mendonça, J. P. R. F., Lesche, B. (2004). Determination of Absolute Values of Refractive Index of Liquids Using an Interferometric Method, *Revista de Física Aplicada e Instrumentacao* 17, June 2004, 74-79, ISSN 0102-6895
- Vest, C. M. (1979), *Holographic Interferometry*, Wiley, ISBN 0-471-90683-2, New York
- Yamaguchi I., Ohta, S., Kato, J.-I. (2001). Surface contouring by phase-shifting digital holography, *Optics and Lasers in Engineering* 36, November 2001, 417-428, ISSN 0143-8166

IntechOpen



## **Holography, Research and Technologies**

Edited by Prof. Joseph Rosen

ISBN 978-953-307-227-2

Hard cover, 454 pages

**Publisher** InTech

**Published online** 28, February, 2011

**Published in print edition** February, 2011

Holography has recently become a field of much interest because of the many new applications implemented by various holographic techniques. This book is a collection of 22 excellent chapters written by various experts, and it covers various aspects of holography. The chapters of the book are organized in six sections, starting with theory, continuing with materials, techniques, applications as well as digital algorithms, and finally ending with non-optical holograms. The book contains recent outputs from researches belonging to different research groups worldwide, providing a rich diversity of approaches to the topic of holography.

### **How to reference**

In order to correctly reference this scholarly work, feel free to copy and paste the following:

Eduardo Acedo Barbosa (2011). Real-time, Multi-wavelength Holographic Recording in Photorefractive Volume Media: Theory and Applications, Holography, Research and Technologies, Prof. Joseph Rosen (Ed.), ISBN: 978-953-307-227-2, InTech, Available from: <http://www.intechopen.com/books/holography-research-and-technologies/real-time-multi-wavelength-holographic-recording-in-photorefractive-volume-media-theory-and-applicat>

**INTECH**  
open science | open minds

### **InTech Europe**

University Campus STeP Ri  
Slavka Krautzeka 83/A  
51000 Rijeka, Croatia  
Phone: +385 (51) 770 447  
Fax: +385 (51) 686 166  
[www.intechopen.com](http://www.intechopen.com)

### **InTech China**

Unit 405, Office Block, Hotel Equatorial Shanghai  
No.65, Yan An Road (West), Shanghai, 200040, China  
中国上海市延安西路65号上海国际贵都大饭店办公楼405单元  
Phone: +86-21-62489820  
Fax: +86-21-62489821

© 2011 The Author(s). Licensee IntechOpen. This chapter is distributed under the terms of the [Creative Commons Attribution-NonCommercial-ShareAlike-3.0 License](#), which permits use, distribution and reproduction for non-commercial purposes, provided the original is properly cited and derivative works building on this content are distributed under the same license.

IntechOpen

IntechOpen